

On-site background measurements for the J-PARC E56 experiment: A search for the sterile neutrino at J-PARC MLF

S. Ajimura¹, T. J. C. Bezerra², E. Chauveau², T. Enomoto², H. Furuta², M. Harada³, S. Hasegawa³, T. Hiraiwa¹, Y. Igarashi⁴, E. Iwai⁴, T. Maruyama^{4,*}, S. Meigo³, T. Nakano¹, M. Niiyama⁵, K. Nishikawa⁴, M. Nomachi¹, R. Ohta^{4,†}, H. Sakai², K. Sakai³, S. Sakamoto³, T. Shima¹, F. Suekane², S. Y. Suzuki⁴, K. Suzuya³, and K. Tauchi⁴

¹Research Center for Nuclear Physics, Osaka University, 10-1, Mihogaoka, Ibaraki, Osaka 567-0047, Japan

²Research Center for Neutrino Science, Tohoku University, 6-3, Aza-aoba, Aramaki, Aoba-ku, Sendai, Miyagi 980-8578, Japan

³J-PARC Center, JAEA, 2-4, Shirane, Shirakata, Naka, Ibaraki 319-1106, Japan

⁴High Energy Accelerator Research Organization (KEK), 1-1, Oho, Tsukuba, Ibaraki 305-0801, Japan

⁵Department of Physics, Kyoto University, Kitashirakawa Oiwake, Sakyo-ku, Kyoto 606-8502, Japan

*E-mail: takasumi.maruyama@kek.jp

Received February 23, 2015; Revised April 22, 2015; Accepted May 7, 2015; Published June 22, 2015

.....
The J-PARC E56 experiment aims to search for sterile neutrinos at the J-PARC Materials and Life Science Experimental Facility (MLF). In order to examine the feasibility of the experiment, we measured the background rates of different detector candidate sites, which are located at the third floor of the MLF, using a detector consisting of plastic scintillators with a fiducial mass of 500 kg. The gammas and neutrons induced by the beam as well as the backgrounds from the cosmic rays were measured, and the results are described in this article.
.....

Subject Index C32

1. Introduction

We proposed a definite search for the existence of neutrino oscillations with Δm^2 near 1 eV^2 at the J-PARC Materials and Life Science Experimental Facility (MLF) [1]. With the 3 GeV Rapid Cycling Synchrotron (RCS) and a spallation neutron target, an intense neutrino beam from muon decay at rest (μDAR) is available. Neutrinos come predominantly from the μ^+ decay: $\mu^+ \rightarrow e^+ + \bar{\nu}_\mu + \nu_e$. The oscillation to be searched for is $\bar{\nu}_\mu \rightarrow \bar{\nu}_e$, which is detected by the inverse β decay (IBD) interaction $\bar{\nu}_e + p \rightarrow e^+ + n$, followed by gammas from neutron capture. Figure 1 (left) shows a bird's-eye view of the MLF building.

The unique features of the proposed experiment, compared with the prior LSND experiment [2] and experiments using conventional horn-focused beams (e.g., [3]), are:

- (1) The pulsed proton beam with about 600 ns spill width from J-PARC RCS and muon long lifetime allows us to select neutrinos from μDAR (the protons are produced with a repetition rate of 25 Hz, where each spill contains two 100 ns-wide pulses of protons spaced 600 ns apart).

[†]Now at Quintessa K.K., Kanagawa, Japan.

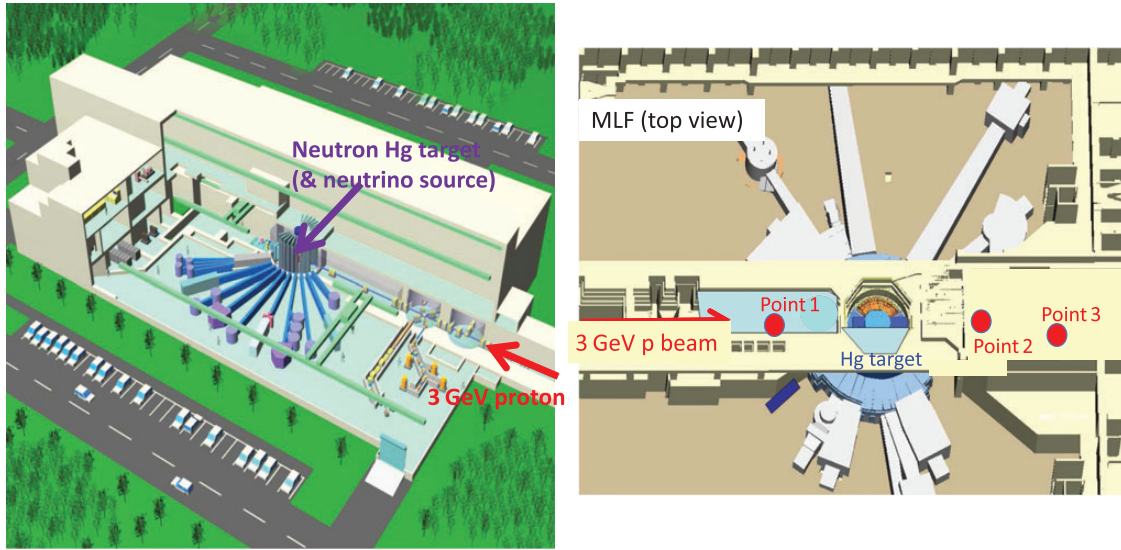


Fig. 1. A bird's-eye view of the the MLF facility in J-PARC (left), and the measurement locations (red circles) of the experiment (right; those are written as "Point 1," "Point 2," and "Point 3").

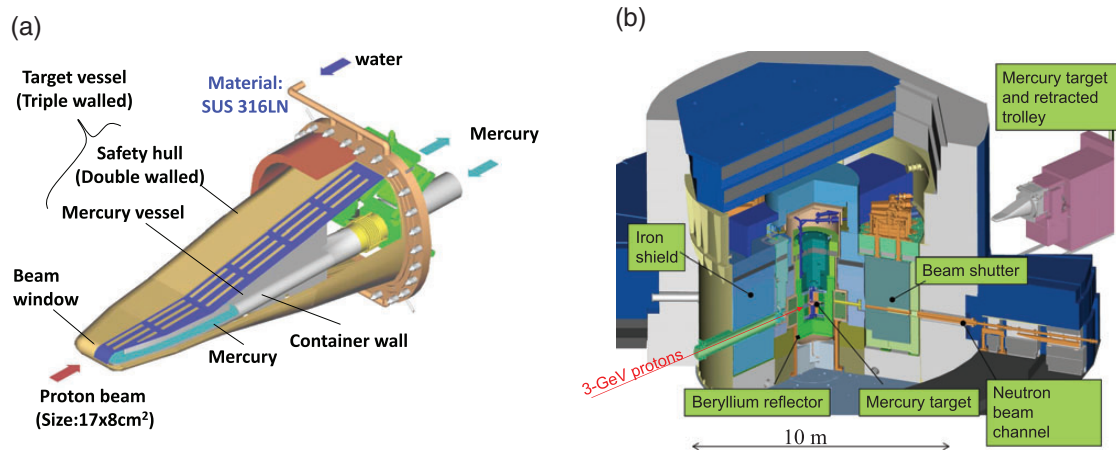


Fig. 2. Mercury target (left) and the structure, which surrounds the target (right).

This can be easily achieved by gating out for about $1 \mu\text{s}$ from the start of the proton beam spill, that eliminates neutrinos from pion and kaon decay in flight.

- (2) The time gate width with $\sim 10 \mu\text{s}$ to obtain the neutrinos from μDAR can also provide superb rejection capability on the cosmic ray background by a factor of ~ 4000 .
- (3) The spallation neutron source is the mercury target, which is a high- Z material, surrounded by thick iron and concrete shields as shown in Fig. 2. Due to a strong nuclear absorption of π^- and μ^- in the mercury target, neutrinos from μ^- decay are strongly suppressed up to about the 10^{-3} level. The resulting neutrino beam is predominantly ν_e and $\bar{\nu}_\mu$ from μ^+ with contamination from other neutrino species at the level of 10^{-3} .
- (4) $\bar{\nu}_e$ interacts via IBD and its cross section is known to a few percent accuracy [4].
- (5) The neutrino energy can be reconstructed from the positron visible energy by adding $\sim 0.8 \text{ MeV}$.
- (6) The $\bar{\nu}_\mu$ and ν_e fluxes have different and well-defined spectra. This allows us to separate $\bar{\nu}_e$ due to $\bar{\nu}_\mu \rightarrow \bar{\nu}_e$ oscillations from those due to μ^- decay contamination.

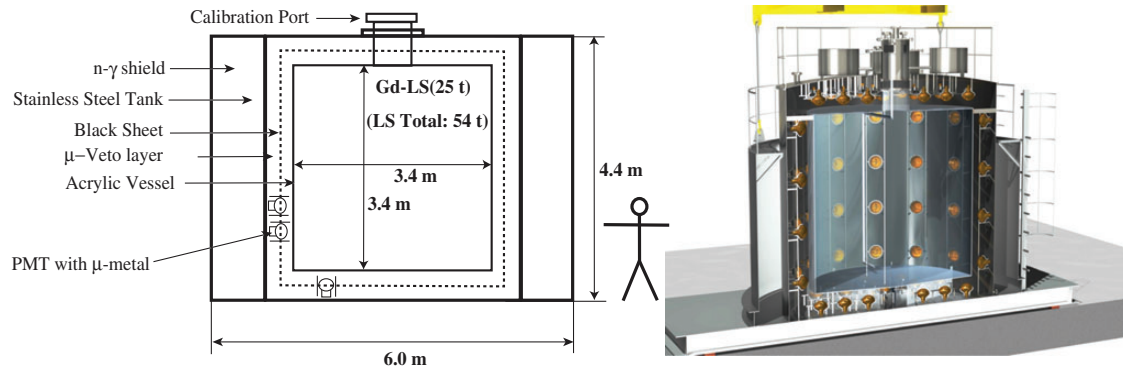


Fig. 3. Current design of the E56 25 ton detector. Left: schematic view; right: 3D drawings.

In addition to these, a Gd-loaded liquid scintillator [5] is used to reduce the accidental backgrounds in the E56 experiment. Figure 3 shows the current detector design.

In the proposal, two detectors are placed on the third floor of MLF with a baseline ~ 20 m from the mercury target.

In order to examine the feasibility of the J-PARC E56 experiment, we carried out an on-site test experiment (MLF 2014BU1301 experiment), which was mainly dedicated to measuring the beam-related backgrounds. The required accuracy of the measurements is a few tens % to check the feasibility of the E56. The data was taken from April to July 2014 using a 500 kg plastic scintillator. The setup and calibration of the detector, and the results of background rate measurements are described in this article.

2. Definition of the IBD signal

Before describing the results, the definition of the IBD signal inside the liquid scintillator is clarified since it will be used often within the text. As explained before, the IBD interaction is $\bar{\nu}_e + p \rightarrow e^+ + n$, followed by gammas from the neutron capture. For the detection of the positron, which we call the “prompt signal region,” the energy is selected to be $20 < E < 60$ MeV and the hit time of the activity inside the detector to be $1 < T < 10$ μ s, where T is the time from the proton beam start timing. These criteria are based on the features of the μ DAR neutrinos. On the other hand, to catch the delayed gamma (called the “delayed signal region”), we select activities with energy in the range $7 < E < 12$ MeV and the hit time to be < 100 μ s.

To examine the background rate, these selection criteria are used unless noted otherwise.

3. Plastic scintillators with 500 kg fiducial volume (the 500 kg detector)

The 500 kg plastic scintillator detector consists of the main target scintillators and two layers of the charged particle vetoing system. We describe the setup, the calibration, and the obtained resolution of the scintillator detector in the following subsections.

3.1. Setup

Figure 4 shows a schematic view of the 500 kg plastic scintillator counters placed at the third floor of MLF. The yellow parts of Fig. 4 show the 500 kg main scintillators in this experiment. They consist of two types of scintillators: 12 pieces of $11.7/13.7$ (trapezoid) $\times 7.6 \times 182$ cm³ scintillator (1D) and

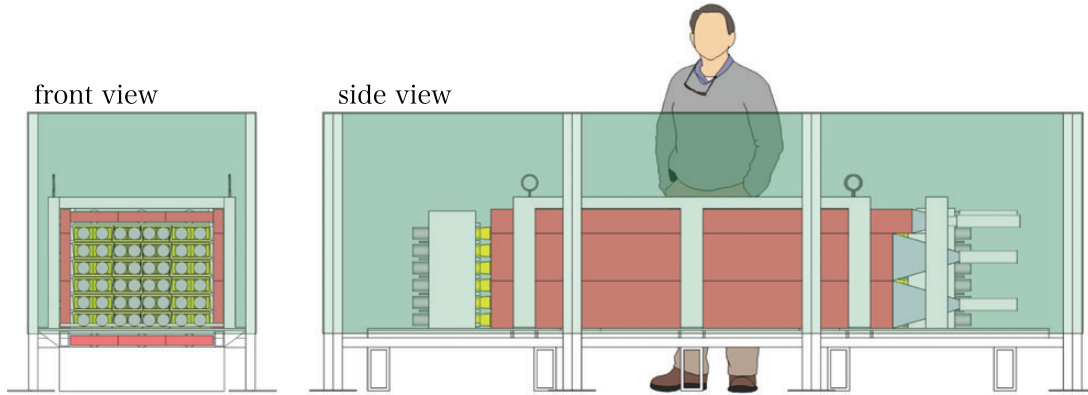


Fig. 4. Schematic view of the 500 kg plastic scintillator detector at the third floor of MLF (left: front view; right: side view). The 500 kg plastic scintillators (yellow) were surrounded by two layers of charged particle vetoing system, the Inner veto (red) and the Outer veto (green).

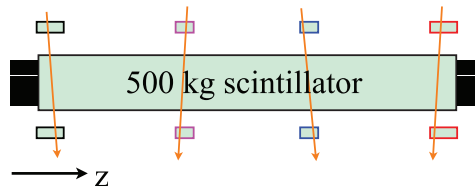


Fig. 5. Schematic view of the cosmic muon trigger counters. Four pairs of plastic scintillators were prepared to trigger cosmic muons.

12 pieces of 16.9/18.8 (trapezoid) \times 7.6 \times 182 cm³ scintillator (3D). To minimize the dead space, 3D scintillators were located on the both sides, while 1D scintillators were located in the central part. Each end of the scintillators was viewed by two PMTs. Signals from each PMT were recorded by a FINESSE 500 MHz 8-bit FADC [6]. The 500 kg detector was surrounded by two layers of charged particle vetoing systems, the Inner and Outer vetoes. The Inner veto (the red parts in Fig. 4) covers the surfaces of the top, bottom, and both sides of the 500 kg detector. The thickness of the plastic scintillator for the Inner veto is 4.3 cm. The Outer veto (the green parts in Fig. 4) surrounds the 500 kg detector and Inner veto, with mostly two layers of 6–8 mm thick plastic scintillators. PMT signals from the veto counters were recorded by a FINESSE 65 MHz FADC with 50 ns RC-filter [6].

3.2. Calibration

We used cosmic muons to calibrate the energy and timing and to measure the attenuation length of the scintillator. Four pairs of plastic scintillators were prepared to define the cosmic ray tracks. Figure 5 shows a schematic view of the cosmic muon trigger counters. The size of the scintillators located at both sides are 132 cm (length) \times 10.5 cm (width) \times 4.0 cm (thickness), while those located in the center are typically 80 cm (length) \times 5.0 cm (width) \times 1.5 cm (thickness).

To measure the attenuation length of the scintillators, we made some dedicated runs in which we changed the position of the trigger counters. Figure 6 shows the typical attenuation curves measured for each scintillator type. We measured the attenuation curve and parametrized for each scintillator. By considering the attenuation length, the reconstructed charge becomes independent from the incident position.

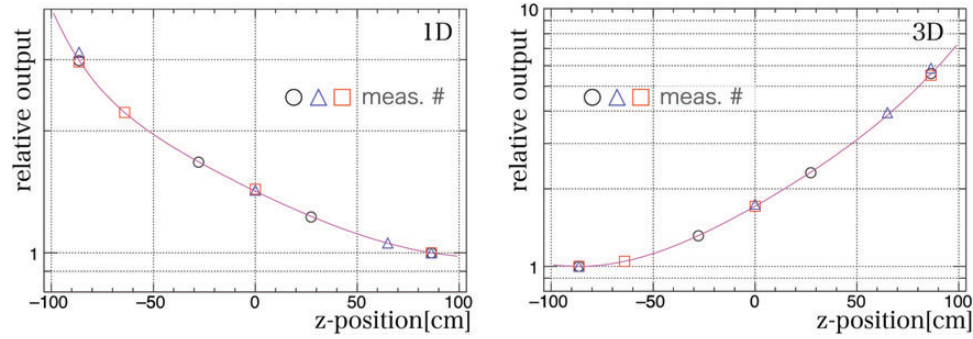


Fig. 6. Typical attenuation curve for each scintillation type (1D and 3D). We measured the curves and parametrized for each scintillator (magenta line; the fit function is the 2nd polynomial + exponential).

The gain of each PMT was also calibrated by using cosmic ray events. The output from each scintillator is stable within 1%–2% during the measurements with the gain correction.

We also adjusted the timing of each PMT. Time offsets were determined to minimize the time difference between each pair of PMTs on each end. The velocity of cosmic muons passing through the detector was considered, where the typical light velocity inside the scintillators is 14.3 cm ns^{-1} .

3.3. Resolutions

We also evaluated the position and energy resolutions of the 500 kg detector using the cosmic ray events. As a result of the precise timing calibrations, the obtained position resolution is $\sigma_z = 2.6 \text{ cm}$ for MIP energy. The typical energy resolutions of the scintillators are 3.3% for 1D and 4.5% for 3D at the middle of the scintillators for MIP energy, which is about 13 MeV.

3.4. Detector simulation

The resolutions described above, and other detector responses such as quenching effects with Birks' law, light attenuation, and the threshold effect, were implemented in a Geant4-based [7,8] Monte Carlo (MC) simulation.

3.5. Veto efficiency

In order to measure the efficiency of the Inner Veto (IV) and Outer Veto (OV) systems on the background measurement, their particle tagging efficiency was measured. The veto efficiency (ε) is defined as follows:

$$\varepsilon_{\text{IV}} = \frac{\text{N of coincident event OV, IV, and Target (Triple Coincidence)}}{\text{N of coincident event OV and Target (Double Coincidence)}}$$

$$\varepsilon_{\text{OV}} = \frac{\text{N of coincident event OV, IV, and Target (Triple Coincidence)}}{\text{N of coincident event IV and Target (Double Coincidence)}}$$

The energy spectra of the main 500 kg detector for different veto conditions in no beam period are displayed in Fig 7. Around the 80 MeV region of the energy distribution without veto, there is a peak created by the cosmic muons. Finally, the veto efficiency for different energy ranges is summarized in Table 1, where it can be seen that the total veto efficiency is better than 99.8%, assuming that the IV and OV inefficiencies are independent. In Table 1 and Fig. 7, it is also possible to see that muons deposit an energy larger than 60 MeV, and most of the cosmic ray muon background is thus rejected.

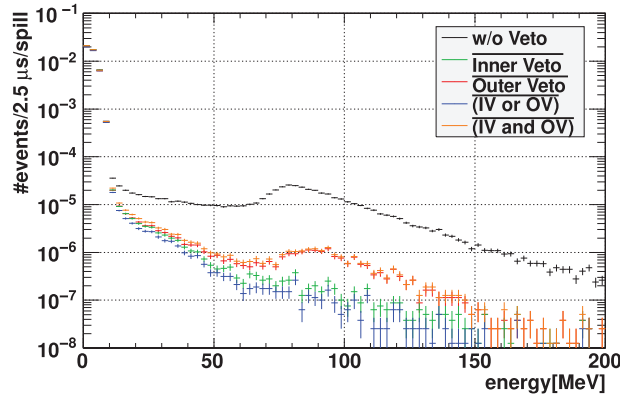


Fig. 7. Energy spectra for the 500 kg detector for different veto conditions. The peak due to the cosmic muons is seen around 80 MeV for the distribution without veto.

Table 1. Summary of IV and OV efficiency for different energy ranges.

Energy Range [MeV]	ε_{IV}	ε_{OV}	(IV or OV)
$20 < E < 60$	$96.8 \pm 0.2\%$	$94.1 \pm 0.2\%$	$\sim 99.8\%$
$60 < E < 100$	$99.5 \pm 0.04\%$	$96.2 \pm 0.1\%$	$\sim 99.9\%$
$100 < E < 140$	$99.6 \pm 0.07\%$	$95.1 \pm 0.3\%$	$\sim 99.9\%$

4. Background measurement locations

Figure 1 shows the overview of the MLF building (left) and the measurement locations (right). The 500 kg detector was moved to measure the backgrounds at each point. The baselines from the mercury target are ~ 17 m, ~ 20 m, ~ 34 m for “Point 1,” “Point 2,” and “Point 3” in Fig. 1, respectively. We accumulated data for two weeks per each point.

Only the results for “Point 2” and “Point 3” are described in this article. The results for “Point 1” are expected to be published later since the analysis is complicated due to a large amount of neutron background.

The number of spills while the beam was used for the analysis were 19,545,739 for “Point 2” and 26,225,816 for “Point 3”, respectively.

5. Fast neutron background from beam

One of the main purposes of the background measurement is to measure the Michel electron background induced by the beam fast neutrons, which was indicated by the previous background measurement at the first floor of the MLF building [1]. According to Geant4, fast neutrons whose kinetic energy is larger than 200 MeV can produce charged pions. The charged pions create Michel positrons, which have the same energy and hit timing as IBD events in the $\pi \rightarrow \mu \rightarrow e$ decay chain, and the scattered fast neutrons are thermalized and captured by Gd. Therefore, this could be a serious correlated background for the E56 experiment. The flux of such fast neutrons at the third floor of MLF was estimated to be some orders of magnitude smaller than that on the first floor [1]. We briefly describe the basic idea and background of this measurement.

Figure 8 shows the definitions of the “signal” and “background” of this measurement. The signal is a Michel electron induced by beam fast neutrons. Fast neutrons coming on the (proton) beam bunch timing hit our detector and produce pions. These pions then produce Michel electrons in the decay chain of $n + p$ (or C) $\rightarrow X + \pi^+$, then $\pi^+ \rightarrow \mu^+ \rightarrow e^+$. The signature of the signal is thus the

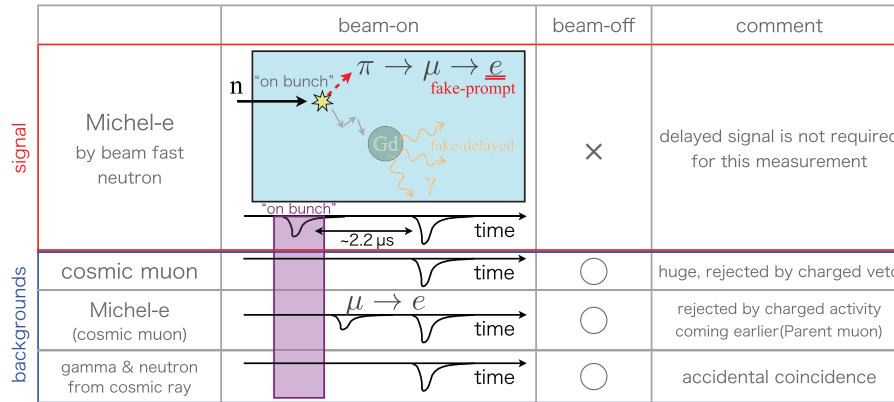


Fig. 8. The definition of “signal” and “backgrounds” for this measurement. Signal is a Michel electron induced by beam fast neutrons. Backgrounds are clipping cosmic muons, Michel electrons from cosmic muons, and neutral particles from cosmic rays.

coincidence between an activity without any veto hits on the bunch timing and a “prompt signal” about $2.2 \mu\text{s}$ later from the beam timing. Backgrounds for this measurement are clipping cosmic muons, Michel electrons from cosmic muons, and neutral particles (gammas and neutrons) from cosmic rays, as shown in Fig. 8, and they come either during beam-on or beam-off. On the other hand, the signal comes only when the beam is on. The basic idea of this measurement is thus to extract signals from backgrounds by subtracting beam-off activities from beam-on activities.

Based on the concept of the measurement, we took the following data set:

- beam-on: To observe activities on the beam bunch and around the bunch timing (the timing definition is described later).
- beam-off (off-timing): To subtract backgrounds from beam-on data. We took data 20 ms after each beam bunch spill. Because detector responses such as the PMT gains, efficiency of veto counters, and others are exactly the same as the last beam spill, we can subtract the backgrounds from the beam signals without systematic uncertainties.
- no-beam: When the accelerator is off. To evaluate truly beam-unrelated background.
- cosmic muons: To calibrate the detector.

Note that the radio frequency (RF) of the RCS provides the beam timing signal for the measurement, thus we used it to take data around the beam and 20 ms later. For the no-beam data, the clock trigger was used.

5.1. Measurement

The search for beam neutrons which induce Michel electrons was performed by detecting their prompt signals. Figure 9 (a) and (b) show the correlation between the energy and the timing of the events observed at “Point 2” and “Point 3.” The zero of the horizontal axis corresponds to the starting time of the proton beam. We observed a large number of activities around the beam time, however the number of activities decreased rapidly as a function of time. No-beam data is also shown in Fig. 9 (c) for comparison. Here we used the clock trigger, so the time axis is arbitrary. In this measurement the prompt signal is defined by:

- $20 < E [\text{MeV}] < 60$
- $1.75 < t [\mu\text{s}] < 4.65$ from the rising edge of the first beam bunch.

to estimate the number of activities in the IBD prompt region.

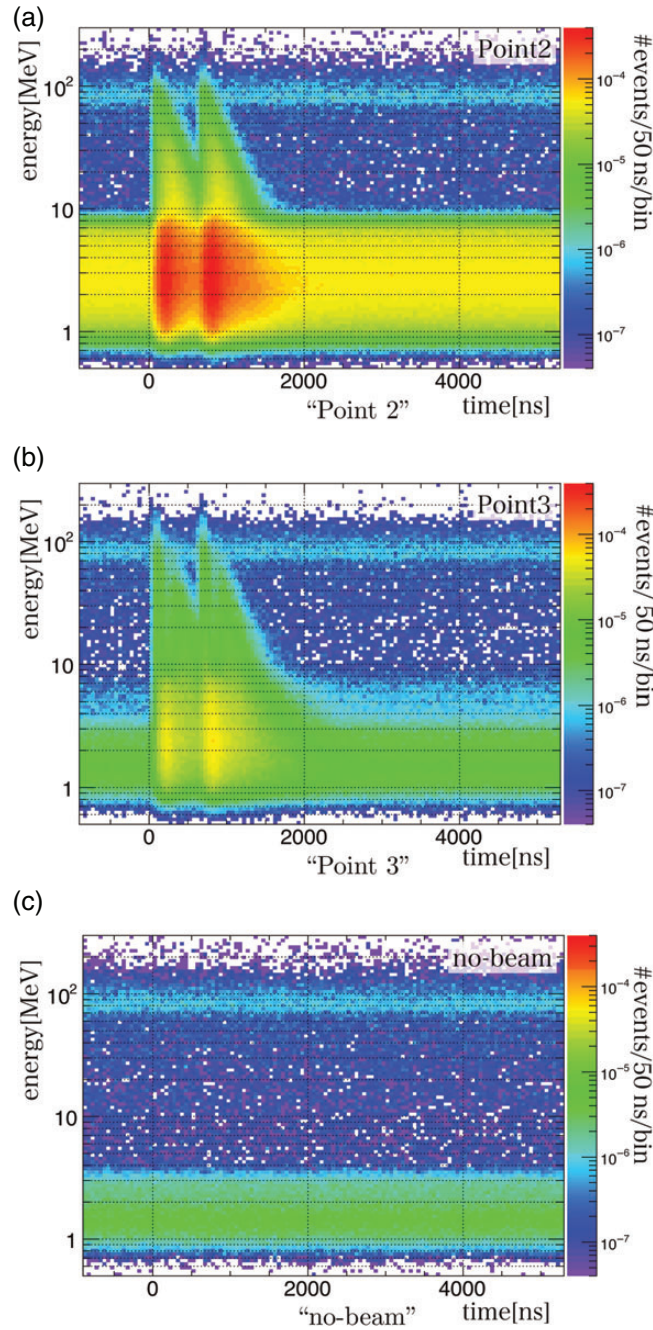


Fig. 9. Correlation between energy and timing of the events observed at (a)“Point 2,” (b)“Point 3,” and (c) “no-beam.” Note that the vertical axis of the two-dimensional plot has a log scale, and one bin of the vertical axis is divided equally in the log scale.

As described before, we compare the beam-on and beam-off data to subtract other activities without any systematic uncertainties. A huge number of clipping muon background events (of the order of a few 100 Hz) were rejected by applying the charged veto cut. Figure 10 shows the energy distributions of events in the prompt timing window, $1.75 < t [\mu\text{s}] < 4.65$ from the beam bunches, and beam-off data, before and after applying the charged veto cut. The observed rates are summarized in Table 2. The numbers of events in the prompt energy range are consistent statistically between beam-on and beam-off data either with or without applying the charged veto cut.

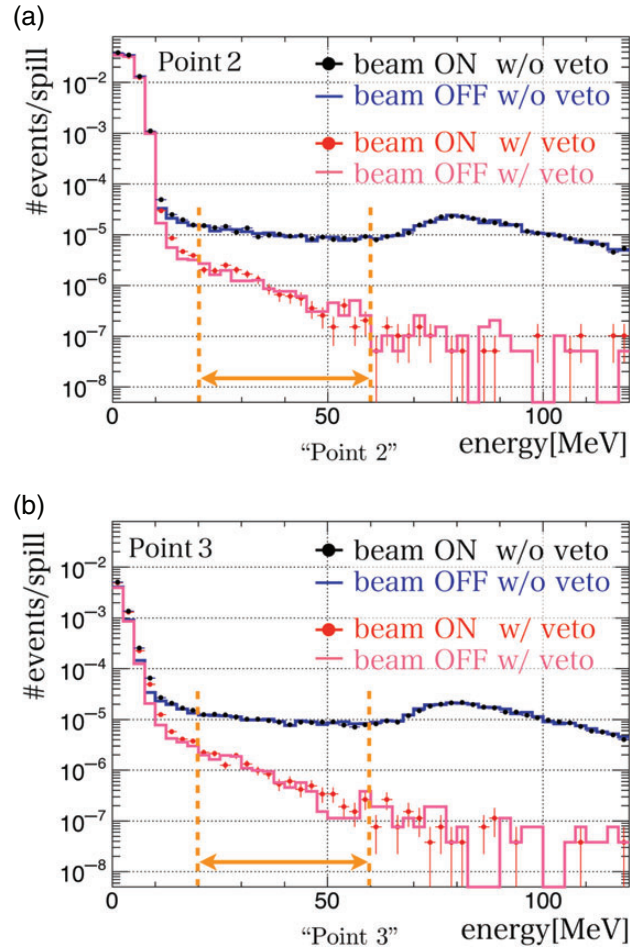


Fig. 10. Energy distributions of events in the prompt timing window and beam-off data, before and after applying the charged veto cut. (a) “Point 2” and (b) “Point 3.”

Table 2. Summary of the background rates in the prompt region.

	“Point 2” ($\times 10^{-5}$ /spill)	“Point 3” ($\times 10^{-5}$ /spill)
Beam-on w/o veto	16.8 ± 0.3	15.3 ± 0.2
Beam-off w/o veto	16.4 ± 0.3	15.4 ± 0.2
Subtraction (on-off)	0.4 ± 0.4	-0.1 ± 0.3
Beam-on w/ veto	1.58 ± 0.09	1.41 ± 0.07
Beam-off w veto	1.52 ± 0.09	1.33 ± 0.07
Subtraction (on-off)	0.06 ± 0.13	0.08 ± 0.10

To improve the sensitivity, an additional cut was applied before obtaining the final result. Figure 11 shows a simulated energy distribution on the bunch timing when fast neutrons produce charged pions in the 500 kg detector. We can expect some events on the bunch timing associated with beam Michel electron backgrounds.

On the other hand, as shown in Fig. 8, the beam-unrelated backgrounds have no activities on the bunch timing. Michel electrons from cosmic muons can have an activity on the bunch timing only when the parent muon comes on the bunch timing accidentally. However, since the muon is a charged particle, it can be easily rejected by the veto counters. We can thus strongly suppress backgrounds

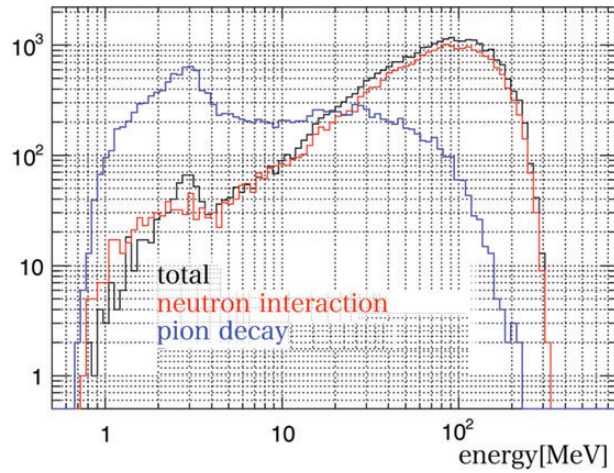


Fig. 11. Energy deposit on the bunch timing for beam Michel electrons with neutron kinetic energy of 300 to 500 MeV (flat). Note this is MC. Red, blue, and black lines are the energy deposit from neutron interactions, pion decays, and their sum in each event. Note that one bin of the horizontal axis is divided equally in the log scale, and the unit of the vertical axis is arbitrary. A peak around 3 MeV in the blue histogram corresponds to the muon kinetic energy, 4.2 MeV, from stopped pion decay including the quenching effects with Birks' law. The quenching effects, light attenuation in the scintillator, and other detector responses such as resolutions and threshold effects are implemented in Geant4 as described in Sect. 3.4.

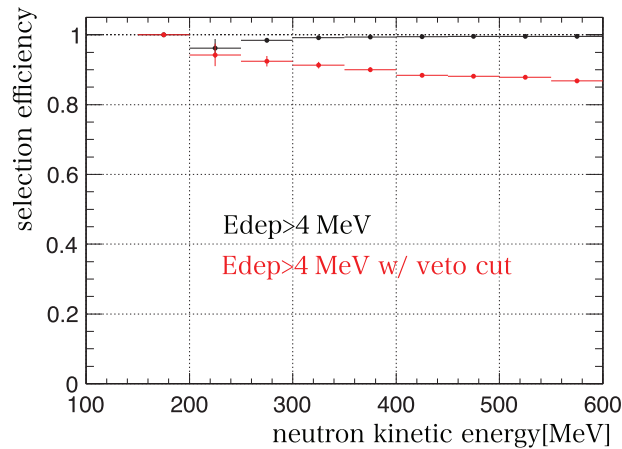


Fig. 12. Estimated selection efficiency of the on-bunch cut as a function of the incident neutron kinetic energy.

by requiring on-bunch activities without hits in the veto counters, and at least one on-bunch activity ($E_{\text{dep}} > 4 \text{ MeV}$) with these veto conditions was required. Figure 12 shows the estimated selection efficiency of this on-bunch cut as a function of the incident neutron kinetic energy based on MC. Though most of the events have more than 4 MeV energy deposit on the bunch timing, some of the events are rejected by self-vetoing. The selection efficiency has a slight dependence on the incident neutron kinetic energy. Because we do not know the energy spectrum of the incident neutron accurately, we assumed a selection efficiency of $\epsilon_{\text{onbunch}} = 0.9$.

Figure 13 shows the energy distributions after applying the cut to the 500 kg detector data. The beam-unrelated distribution was obtained with the energy distribution of beam-off data without applying the on-bunch cut, and the accidental coincidence probability: hit rate of neutral activities on the bunch timing. The mean hit rates without veto activities on the bunch timing

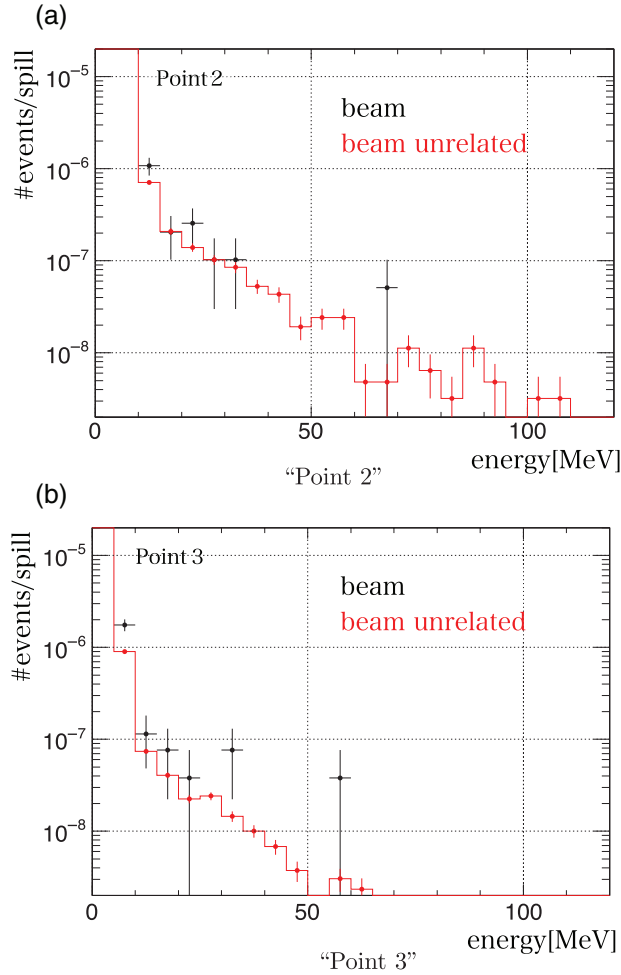


Fig. 13. Energy distributions after applying the on-bunch cut. The beam-unrelated distribution was obtained with the accidental coincidence probability 3.1% (“Point 2”) and 0.6% (“Point 3”), and the energy distribution of beam-off data without applying the on-bunch cut.

Table 3. Summary of the background rates in the prompt region after the on-bunch cut.

	“Point 2” ($\times 10^{-7}/\text{spill}$)	“Point 3” ($\times 10^{-7}/\text{spill}$)
Beam-on data	4.60 ± 1.53	1.53 ± 0.76
Prediction	4.91 ± 0.28	0.86 ± 0.04
Subtraction	-0.31 ± 1.56	0.67 ± 0.76
90% C.L. upper limit	<2.5	<2.1

were 3.1% (“Point 2”) and 0.6% (“Point 3”). The observed event rates during beam-on were $(4.60 \pm 1.53) \times 10^{-7}/\text{spill}$ (“Point 2”) and $(1.53 \pm 0.76) \times 10^{-7}/\text{spill}$ (“Point 3”), while the estimated event rate by beam-unrelated activities were $(4.91 \pm 0.28) \times 10^{-7}/\text{spill}$ (“Point 2”) and $(0.86 \pm 0.04) \times 10^{-7}/\text{spill}$ (“Point 3”), and both rates between the observed and predicted numbers are consistent. By considering the efficiency of the on-bunch cut, $\epsilon_{\text{onbunch}} = 0.9$, the upper limit of the event rate of the beam Michel electron are thus $2.5 \times 10^{-7}/\text{spill}$ (90% C.L., “Point 2”) and $2.1 \times 10^{-7}/\text{spill}$ (“Point 3”). Table 3 summarizes these numbers.

6. Accidental background

Another important background comes from accidental coincidences. The accidental background rate is estimated using the multiplication of the single rates of the background in the prompt region and that in the delayed region. Therefore absolute rates for the background measurements on the prompt and the delayed region with the 500 kg detector are crucial. Measurements with small size detectors are also important to estimate the contents (particle identification: PID) of the prompt background.

We first explain the background measurements for the prompt region, and then for the delayed region.

6.1. Single background rate measurement for prompt region

As shown in the previous section, the background rates in the prompt region after charged particle veto are consistent statistically between “beam-on” and “beam-off” data. This means that the beam-related background is small enough compared to the beam-unrelated background which is expected to be mainly due to the neutral particles, gammas, or neutrons induced by cosmic rays. Since the response of the E56 detector is quite different for gammas and neutrons, it is essential to estimate their influences separately in the prompt region. Thus measurements of the particle identification for the prompt region were done at Tohoku University using small size detectors at first, which were used to construct and to check the flux model. Finally, the flux model was compared with the 500 kg detector data taken at the third floor of MLF. All details are described in the following subsections.

6.1.1. PID and energy measurements with small size detectors

The calibrations of the small size detectors are described elsewhere [9], so only a summary of the measurements is shown here.

There are no reliable gamma flux measurements or models so far at the ground level, which contributes to the prompt event of the accidental background. High-energy gammas are supposed to be produced mainly by the decay of π^0 which are created by μ -nucleon interactions in the walls of the building or air, outside the detectors. Therefore we constructed an empirical gamma flux model with two very simple exponential functions for energy at the surface of the detector:

$$\frac{dN}{dE_n (\text{MeV})} = \frac{A}{B} \cdot e^{-\frac{E_n}{B}} + \frac{C}{D} \cdot e^{-\frac{E_n}{D}}. \quad (1)$$

Parameters, A , B , C , D were determined from data from a sodium iodide (NaI) detector (a cylinder with 2'' diameter and 2'' height) at Tohoku. Cosmic ray muons were rejected using plastic scintillator anti-counters, which surround the NaI counters, with a veto efficiency better than 99%. Note that the cosmic μ veto also eliminated the gammas from π^0 s created by μ -nucleon interactions inside the detector. This statement can be expanded to any size detectors in general. Figure 14 shows the results of the measurement, where the energy spectrum in the yellow part can be described by two exponential functions with mean energies of 3 (“ A ” in Eq. 1) and 26 MeV (“ B ”; the MC gammas are generated using the two exponential functions from the NaI surface assuming an isotropic direction). Comparing data and MC spectra, these component rates are measured to be 150 (“ C ”) for the first exponential function and 25 Hz m^{-2} (“ D ”) for the second.

Another important measurement had been done using a small liquid scintillator (NE213 [11]) which can separate neutrons from gammas efficiently using the pulse shape of the scintillation light (PSD: pulse shape discrimination). Neutron signals have larger tails than those from gammas, thus we can check the flux of fast neutrons in addition to the gamma flux which was already measured

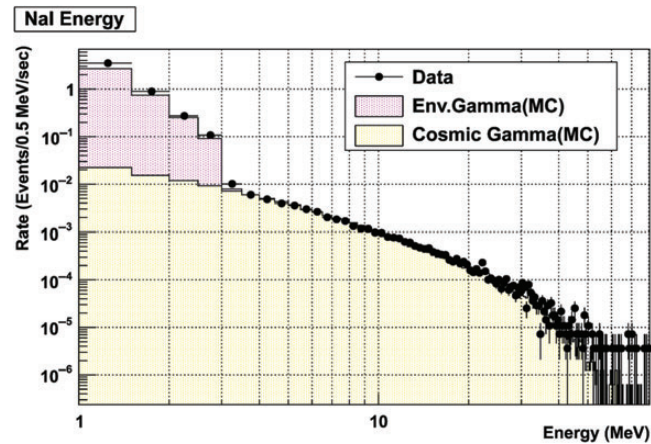


Fig. 14. NaI energy spectrum for the remaining events after applying the veto cut. The environmental gammas below 3 MeV are generated based on Ref. [10]. Note that the horizontal axis is based on a log scale, but one bin of the axis is divided by 0.5 MeV.

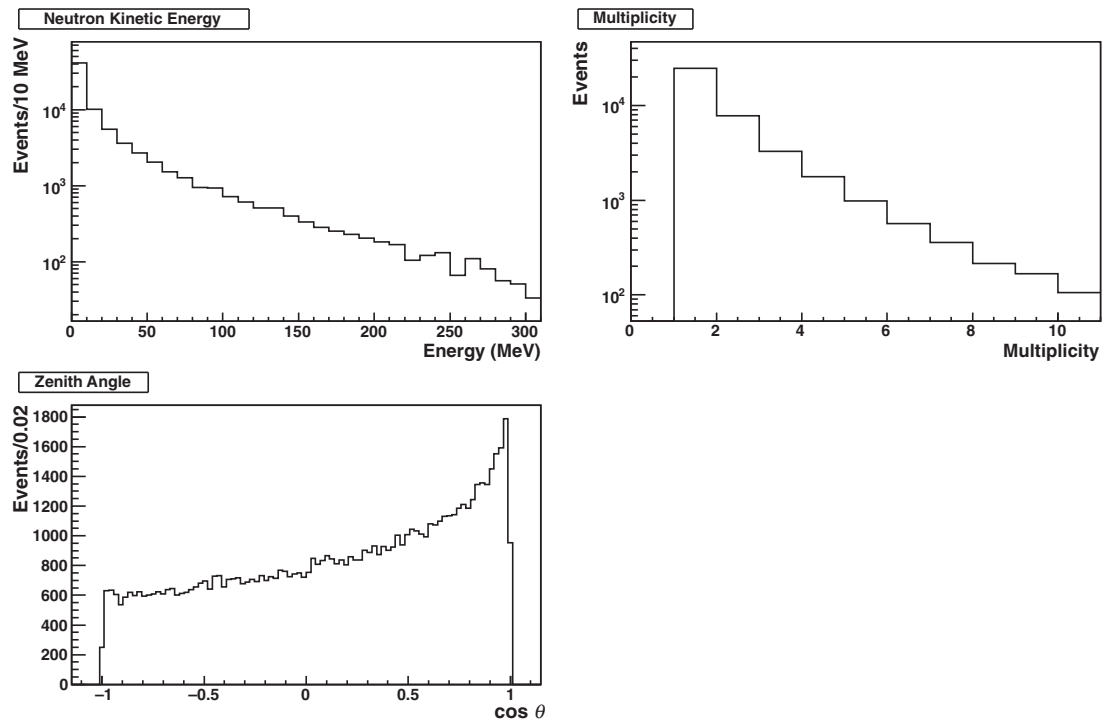


Fig. 15. Distributions of the neutron kinetic energy (upper left plot), multiplicity (upper right plot), and zenith angle (lower plot) of the cosmic muon induced fast neutron events generated by the empirical functions in Ref. [13].

by NaI. Fast neutrons induced by cosmic rays are measured and modeled in some previous works. For this study we employed the model and the parameters given by Wang et al. [13], who gave the empirical functions on the kinetic energy (E_n), the multiplicity (M), and the zenith angle (θ) of the fast neutrons as a function of the muon energy (E_μ). Figure 15 shows these distributions.

A cylindrical aluminum housing (5'' in diameter and 2'' in height), with white painted inner walls, is filled with NE213, closed with a glass plate and attached to a 5'' PMT (R1250-03). The NE213

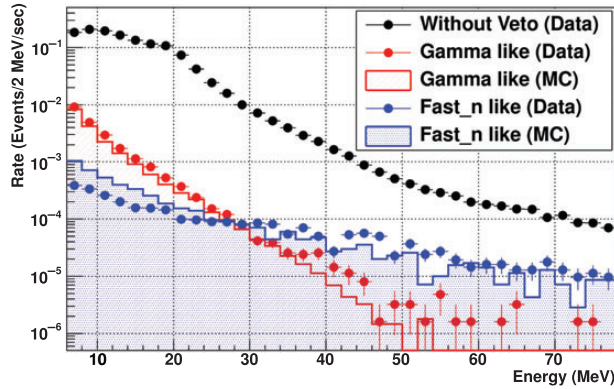


Fig. 16. Reconstructed energy distribution for events with low or no energy deposition in the veto. The data and MC components of neutrons and gammas are also compared. Data events without veto applied are also shown for comparison.

detector was also surrounded by the plastic scintillators, and Fig. 16 shows the results of the measurement.

With this setup, the fast neutron flux detected above 20 MeV was $(1.28 \pm 0.05) \times 10^{-3}$ Hz (statistical uncertainty), while the MC based on Ref. [13] gives a rate of 1.12×10^{-3} Hz. For gammas in the same energy range, the measured rate was $(1.18 \pm 0.04) \times 10^{-3}$ Hz (statistical uncertainty), while the MC based on the NaI measurement described above gives 0.95×10^{-3} Hz. MC simulation generates the gammas at the surfaces of the detectors isotropically. Therefore, the data and MC above 20 MeV for both gammas and neutrons agree within 20% of the uncertainty.

6.1.2. Measurement for prompt background with 500 kg detector

Figure 18 shows the energy distribution of no-beam data after applying the charged particle veto and Michel electron cuts. Because activities induced by cosmic rays are dominant in the prompt region as described above, no-beam data is used to estimate the background for simplicity. The MC estimation with cuts is overlaid. Fast neutrons are generated based on the model in Ref. [13], and the gammas are again generated based on Eq. (1) at the surface of the 500 kg detector isotropically.

Cosmic muons were eliminated by applying the charged particle veto cut because of the high veto efficiency ($> 99.8\%$) as described in Sect. 3.5. The Michel electrons can be rejected by detecting the parent muons coming earlier than the prompt events by 70 ns. Figure 17 shows the timing distribution of parent muons that generate Michel electrons within a time window of $3.9 < t [\mu\text{s}] < 5.4$, based on a toy MC. This time window is applied to the real data observation to obtain Fig. 18. Some of the events within the time window remained after the cut because the Michel electrons came too close to their parent muons (corresponding to the right red-hatched histogram of Fig. 17.) Events in the negative region also remained because they were out of the FADC time window (corresponding to the left red-hatched histogram of Fig. 17). The rejection power of the Michel electron cut was thus estimated to be 7.

After the cuts, the remaining events are composed of cosmic gammas and neutrons, mainly for the prompt region.

The cosmic-induced fast neutrons make the correlated background, however the 25 ton detectors for the E56 will have PID capability, which can reject fast neutrons relative to electrons and gammas by a factor of more than 100 [1]. Neutrons in the remained events are thus not harmful and only

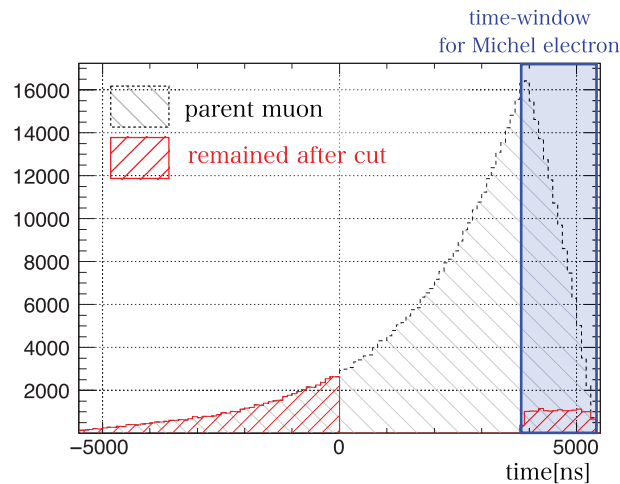


Fig. 17. Timing distribution of parent muons that generate Michel electrons within a time window, obtained by a toy Monte Carlo. The time window for Michel electrons is $3.9 < t [\mu\text{s}] < 5.4$.

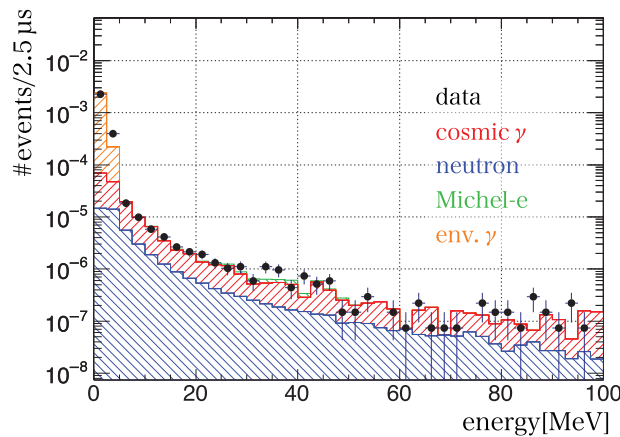


Fig. 18. Energy distribution of no-beam data after applying the charged particle veto cut and the cosmic Michel electron cut.

gammas can be a prompt background. By using the gamma flux model described above, the number of gammas in the remaining events was equivalent to $(6.4 \pm 0.5) \times 10^{-6} (2.5 \mu\text{s})^{-1}$.

Note that the predicted rate from the measurement at Tohoku University was consistent with the rate measured by the 500 kg detector at the MLF within 6%. As mentioned previously, the goal of the test experiment is to check the energy and the rate of the onsite backgrounds. The neutron and gamma flux models in this work can be used to discuss the feasibility of the E56 experiment [9].

6.2. Single background rate measurement for delayed region

There are two dominant backgrounds for the delayed region. They are neutrons and gammas induced by the beam, and are described in the next subsections.

6.2.1. Beam neutrons

Thermal neutrons on the third floor of MLF are not harmful for the E56 experiment since they are stopped at the buffer region of the E56 detector, whose thickness of liquid scintillator is 50 cm (Fig. 3). But the middle energy ($10 \text{ MeV} < E_{\text{kin}}$) neutrons on the beam bunch can be thermalized inside the

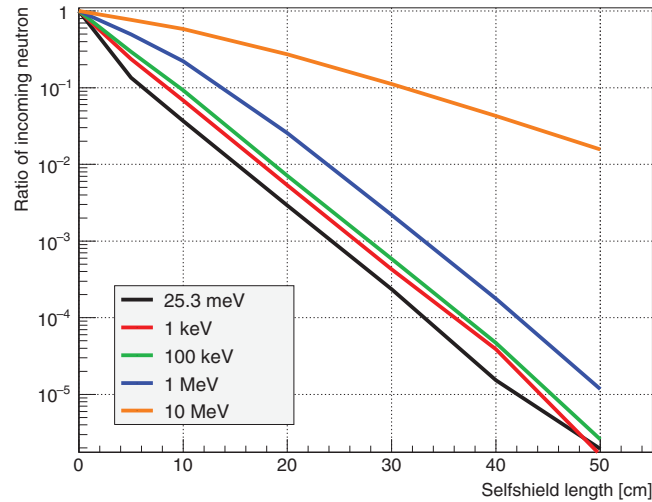


Fig. 19. Self-shield effect of liquid scintillator as a function of the shield thickness.

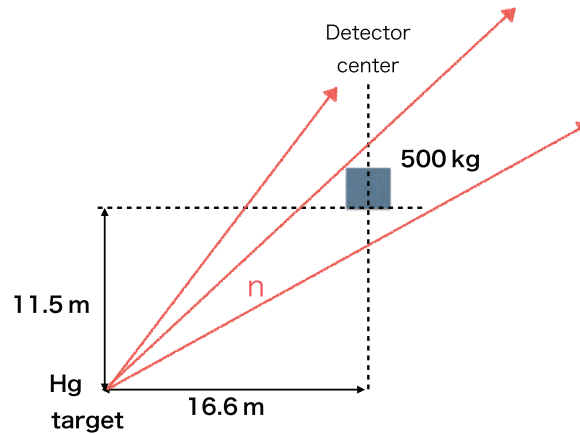


Fig. 20. Geometry of the mercury target and the 500 kg detector.

detector, captured in the liquid scintillator, and emit gammas inside the fiducial volume. They become backgrounds for the delayed region. Figure 19 shows the attenuation rates of thermal neutrons inside the liquid scintillator generated by Geant4. Most of neutrons of less than 10 MeV are rejected at the buffer region.

We estimated the neutron flux on the beam bunch timing above 15 MeV using data assuming the reaction rates of neutrons inside the 500 kg detector based on Geant4 since the beam gammas are dominated below 15 MeV as described later. Here we used the number of activities and their energy spectrum with a time window less than 3 μ s from the beam start time to estimate the flux. The MC simulation also assumed that such fast neutrons are created at the mercury target isotropically and come directly to the 500 kg detector. Figure 20 shows a schematic view of the assumption.

This assumption is only valid for neutron backgrounds with similar solid angle positions since the scattered angle, energy, and production rate are tightly correlated; however, the assumption gives a good shape for “Point 2” and “Point 3” as described later.

The flux, $\phi(E_n)$, is denoted as

$$\phi(E_n) = \frac{\alpha}{30} \exp(-E_n/30), \tag{2}$$

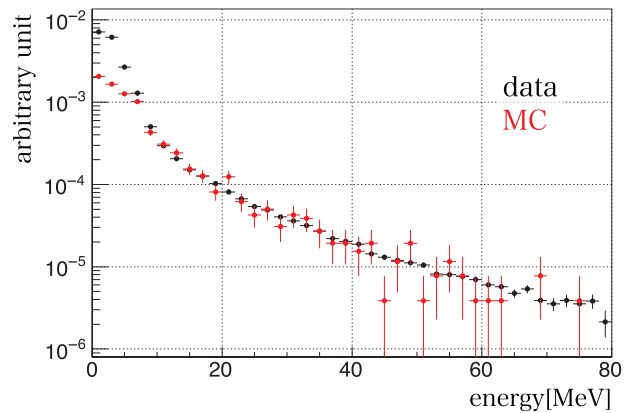


Fig. 21. Energy distribution of the 500 kg detector for on-bunch timing. The black crosses show the measured energy spectrum and the red ones an MC fitted to the measured one.

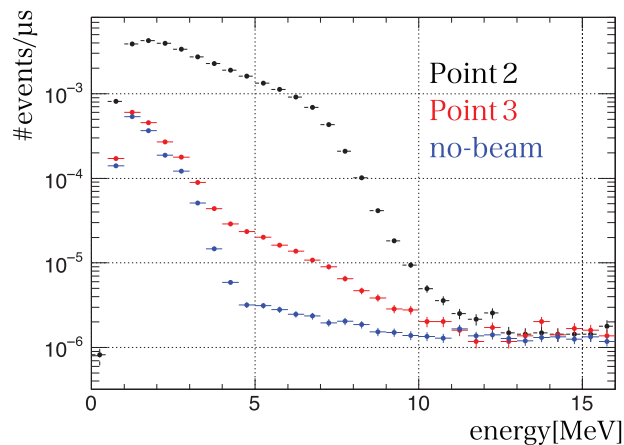


Fig. 22. Energy distribution of the backgrounds for the delayed region measured with the 500 kg detector. Black: energy spectrum at “Point 2,” red: that at “Point 3,” blue: no-beam data.

where E_n is the neutron kinetic energy and α is the number of neutrons that are generated at the mercury target in a spill. Note that α is just an “effective” number of generated neutrons at the target since the 500 kg detector is put on the third floor of MLF, and the neutrons are highly attenuated by the iron or concrete which surrounds the target, as shown in Fig. 2. α is estimated to be $(387 \pm 12)/\text{spill}$ as a fit result at “Point 2.” As shown in Fig. 21, this flux reproduces well the measurements above 15 MeV, which is dominated by activities from neutrons.

The neutron rate at “Point 2” with energy above 15 MeV is $(5.4 \pm 0.02) \times 10^{-3}/\text{spill}/0.3 \text{ MW}/500 \text{ kg}$, while that at “Point 3” is $(2.0 \pm 0.01) \times 10^{-3}/\text{spill}/0.3 \text{ MW}/500 \text{ kg}$. Although the neutron flux depends on the scattering angle from the mercury target, these are well explained by the $1/r^2$ law, where r is the detector baseline, within 5%.

6.2.2. Beam gammas

Beam gammas are produced by capture reactions of the thermalized beam neutrons with the materials of the MLF building such as concrete walls or floors. They are injected into the E56 detector, therefore they are a crucial background in the delayed region.

As shown in Fig. 9(a) and (b), the hit time distributions of the low-energy activities were almost flat. Therefore, rate measurements during even a short time span such as only $1 \mu\text{s}$ are useful to

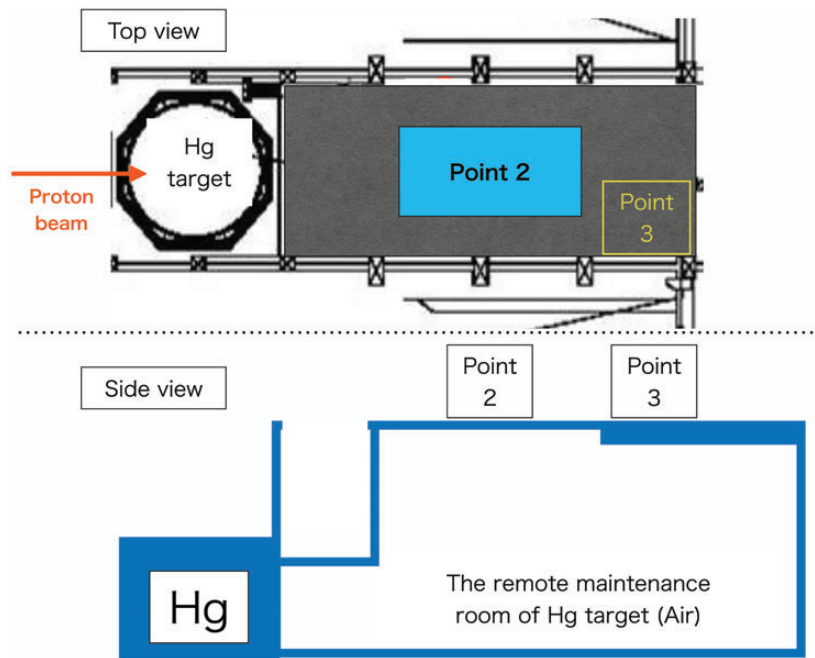


Fig. 23. The top view of the third floor of the MLF around the measurement points. Bottom is the side view. The floor of “Point 2” is made of concrete which has 120 cm thickness and is thinner than that of “Point 3” by 30 cm.

estimate the background rates for the IBD delayed region. Figure 22 shows the energy spectra below 16 MeV measured by the 500 kg detector. $4.35 < t [\mu\text{s}] < 5.35$ from the rising edge of the first beam bunch shown in Fig. 9(a) and (b) were used to estimate background in the IBD delayed region. In the energy region of $7 < E [\text{MeV}] < 12$, the background rates with the 500 kg detector are $(8.26 \pm 0.07) \times 10^{-4}/\mu\text{s}/0.3 \text{ MW}$ at “Point 2,” and $(3.65 \pm 0.12) \times 10^{-5}/\mu\text{s}/0.3 \text{ MW}$ at “Point 3.”

As shown in the bottom plot of Fig 23, there is a room for the remote maintenance of the mercury target under “Point 2” and “Point 3.” The floor of “Point 2” is made of concrete which has 120 cm thickness and is thinner than that of “Point 3” by 30 cm. This structure of the MLF building can make the difference in the background rates between “Point 2” and “Point 3.”

7. Summary

The J-PARC MLF 2013BU1013 test experiment was carried out to measure the backgrounds and to examine the feasibility of the J-PARC E56 experiment. The results show that:

- Beam fast neutrons:

The beam fast neutrons which create charged pions inside the 500 kg plastic scintillators were not observed during two weeks. The 90% C.L. upper limit is set to be $2.5 \times 10^{-7}/2.9 \mu\text{s}/0.3 \text{ MW}$ at “Point 2,” and $2.1 \times 10^{-7}/2.9 \mu\text{s}/0.3 \text{ MW}$ at “Point 3.”
- Accidental:
 - (1) The gammas or neutrons induced by cosmic rays are observed for the prompt region. The neutron rate is the same as expected in Ref. [13]. Gammas are newly recognized by this experiment. The number of gammas is equivalent to $(6.4 \pm 0.5) \times 10^{-6}/2.5 \mu\text{s}$ in the 500 kg detector in the prompt region.
 - (2) Neutrons and gammas induced by the beam are observed for the delayed region by the 500 kg detector. The flux of neutrons is estimated by the data, and the shape of the flux is consistent

with an exponential with a slope constant of 30 MeV. The effective neutron production rate is $(387 \pm 12)/\text{spill}$ at the target. “Point 2” and “Point 3” have the same neutron flux within 5%, considering the baseline effect. The rates of gammas are $(8.26 \pm 0.07) \times 10^{-4}/\mu\text{s}/0.3 \text{ MW}$ (“Point 2”) and $(3.65 \pm 0.12) \times 10^{-5}/\mu\text{s}/0.3 \text{ MW}$ (“Point 3”) in the energy region of $7 < E [\text{MeV}] < 12$.

This information has been translated to the background rates at the E56 detectors using MC simulation with evaluation of the self-shielding effects, and the results show that the backgrounds at “Point 2” provide no specific problems for performing the J-PARC E56 experiment [9].

Acknowledgements

We warmly thank the MLF staff, especially Prof. Masatoshi Arai, who is the MLF Division leader, and the neutron source group, muon group, and user facility group for various kinds of support. The LEPS2 experiment has lent us good quality scintillators, electronics, cables, PMTs, and we deeply appreciate it. We borrowed cables, electronics, scintillators from the J-PARC Hadron group, University of Kyoto, JAEA, KEK online group, Belle II experiment, and T2K experiment and we would like to express appreciation for their kindness. We also thank Bill Louis (LANL), Minfang Yeh (BNL), and Joshua Spitz (MIT) for useful discussions.

Finally, we thank Grant-in-Aid for Scientific Research, J-PARC, KEK, CROSS, JSPS and MEXT for their support.

References

- [1] M. Harada et al., [[arXiv:1310.1437](#) [physics.ins-det]] [[Search INSPIRE](#)].
- [2] A. Aguilar et al., Phys. Rev. D **64**, 112007 (2001).
- [3] A. A. Aguilar-Arevalo et al., Phys. Rev. Lett. **110**, 161801 (2013).
- [4] P. Vogel and J. F. Beacom, Phys. Rev. D **60**, 053003 (1999).
- [5] M. Yeh, A. Garnov, and R. L. Hahn, Nucl. Instrum. Meth. A **578**, 329 (2007).
- [6] Y. Igarashi et al., IEEE Trans. Nucl. Sci. **52**, 2866 (2005).
- [7] J. Alison et al., IEEE Trans. Nucl. Sci. **53**, 270 (2006).
- [8] S. Agostinelli et al., Nucl. Instrum. Meth. A **506**, 250 (2003).
- [9] M. Harada et al., [[arXiv:1502.02255](#) [physics.ins-det]] [[Search INSPIRE](#)].
- [10] H. Furuta et al., Nucl. Instrum. Meth. A **568**, 710 (2006).
- [11] Y. Uwamino, K. Shin, M. Fuji, and T. Nakamura, Nucl. Instrum. Meth. **204**, 179 (1982).
- [12] H. Furuta et al., Proc. 2nd Int. Conf. on ANIMMA, IEEE, Ghent (2011).
- [13] Y-F. Wang, et al., Phys. Rev. D **64**, 013012 (2001).